

Article

Application of Naphthalenediimide Derivatives as Self-Assembled Electron Selective Contacts in CdSe@ZnS Quantum Dots LEDs

Maria Méndez¹, Abarna Sekar², Dylan Wilkinson², Margarita Gracia¹, Andrea Di Vera¹, Laia Marín-Moncusí¹, José G. Sánchez¹, Fabian Pino³, Rafael S. Sánchez³, Iván Mora-Seró³, Michele Cariello², Emilio Palomares^{1,4}, Graeme Cooke^{2,*} and Eugenia Martínez-Ferrero^{1,*}

¹ Institute of Chemical Research of Catalonia-The Barcelona Institute of Science and Technology (ICIQ-BIST), Avda, Països Catalans 16, 43007 Tarragona, Spain

² School of Chemistry, University of Glasgow, Glasgow G12 8QQ, UK

³ Institute of Advanced Materials (INAM), Universitat Jaume I (UJI), Avenida de Vicent Sos Baynat, s/n, 12071 Castelló de la Plana, Spain

⁴ Catalan Institution for Research and Advanced Studies (ICREA), 08010 Barcelona, Spain

* Correspondence: Graeme.Cooke@glasgow.ac.uk (G.C.); emartinez@icqi.es (E.M.-F.); Tel.: +44-0141-330-5500 (G.C.); +34-977920200 (E.M.-F.)

How To Cite: Méndez, M.; Sekar, A.; Wilkinson, D.; et al. Application of Naphthalenediimide Derivatives as Self-Assembled Electron Selective Contacts in CdSe@ZnS Quantum Dots LEDs. *Materials and Sustainability* **2025**, *1*(2), 9. <https://doi.org/10.53941/matsus.2025.100009>.

Received: 19 May 2025

Revised: 27 May 2025

Accepted: 4 June 2025

Published: 10 June 2025

Abstract: Despite the successful application of self-assembled molecules (SAMs) as hole-selective contacts in light-emitting diodes (LEDs), examples of the use of electron-selective SAMs are scarce. Here, we investigate the potential of naphthalene diimide (NDI) as an efficient electron-selective contact in CdSe@ZnS-based LEDs. CdSe@ZnS quantum dots, due to their exceptional optical properties, have found a range of applications in optoelectronics. In particular, they have been widely studied in LEDs because of their stability, tunable and narrow emission, and high photoluminescence quantum yields. In this work, two SAMs based on NDI cores have been synthesized, incorporating different terminal groups to study their structure-device function relationship. **SAM3** contains one carboxylic acid moiety and one long alkyl chain as its substituents, whereas in **SAM12**, both substituents are carboxylic acids. Both inverted (*n-i-p*) and regular (*p-i-n*) device configurations have been explored and analyzed and our results show that the substituents play an important role in controlling device characteristics. Therefore, the application of NDI derivatives as electron selective contacts have been demonstrated opening the door for further research into the underexplored field of electron selective SAMs in optoelectronic devices.

Keywords: naphthalene diimide derivatives; self-assembled molecules; electron-transporting layers; CdSe quantum dots; light-emitting devices

1. Introduction

The application of self-assembled molecules (SAMs) as selective contacts in optoelectronic devices has grown exponentially during the last years due to their ease of application and high efficiency of the devices [1,2]. SAMs are widely used to modify the energy levels and surface energy of metal oxides to which they bind chemically through anchoring groups such as phosphonic or carboxylic acids. As a consequence, the ITO work function is closely aligned with the HOMO/LUMO levels of hole and electron transporting layers, respectively. This energy alignment enhances stability by reducing charge accumulation at the interface and improving the overall charge transport properties of devices [3]. Moreover, SAMs possess chemical stability and exhibit solubility



in organic solvents which facilitates the solution processing with minimal material consumption. There are many examples of SAMs reported for application in solar cells, photodiodes or organic field effect transistors [4–8]. However, in the context of the light emitting diodes (LEDs), the use of SAMs is still quite limited, with only a few studies reported in the literature about their application as hole-selective contacts [9–16]. Moreover, the design and synthesis of efficient electron-selective materials is a significant challenge. For example, Kumar et al. have recently reported the synthesis of triazine derivatives incorporating cyanide groups within their molecular structure and proposed them as potential electron-selective SAMs for LEDs. Although full device fabrication was not carried out as part of proof-of-concept study, the new SAMs were evaluated and found to be highly promising molecular systems for this application [17].

Naphthalene diimide (NDI) is a highly effective electron acceptor group possessing physical and electronic properties that make it a suitable candidate for an electron-transporting layer (ETL). NDI can be chemically modified easily through simple synthetic procedures either at the conjugated backbone or the nitrogen atoms to introduce solubilizing side chains for easy solution processing. Although NDI has been primarily used in the fabrication of air-stable n-type organic field-effect transistors [18,19], it also shows potential as photoactive layer in light-emitting devices (LEDs) and solar cells [20–23], and even as an additive in the electron transport layers of perovskite solar cells [24].

In this work, two NDI-based derivatives named **SAM3** and **SAM12**, both containing the same linker unit to the carboxylic acid moiety, have been synthesized and tested as electron-selective contacts in light-emitting devices. **SAM12**, which contains two carboxylic acid groups at the imide positions, has been previously reported as an ETL in perovskite solar cells [20]. **SAM3**, featuring a single carboxylic acid group, was selected in order to investigate whether this structural change can influence device performance (see Figure 1). To determine whether differences following functionalization in this way influence the performance of light-emitting devices, we fabricated devices using CdSe@ZnS quantum dots (QDs) as the emissive material. These inorganic semiconductor nanocrystals, with sizes ranging between 1 and 15 nm, possess unique light-emitting properties due to the quantum confinement effect induced by their nanometer size that causes high photoluminescence quantum yield, narrow photoluminescence emission peak and color purity. In addition, their chemical stability ensures that the devices are both durable and reproducible. Their application in LEDs has been widely reported and results in devices with low turn-on voltage and high-performance values [25]. Therefore, we have explored the effect of NDI on the performance of both *n-i-p* and *p-i-n* device configurations where the electron selective contact is between the ITO and the emissive layer or between the emissive layer and the top metallic electrode, respectively. The prepared devices are functional in both configurations, yet, **SAM12** delivers higher luminance while **SAM3** higher efficiency.

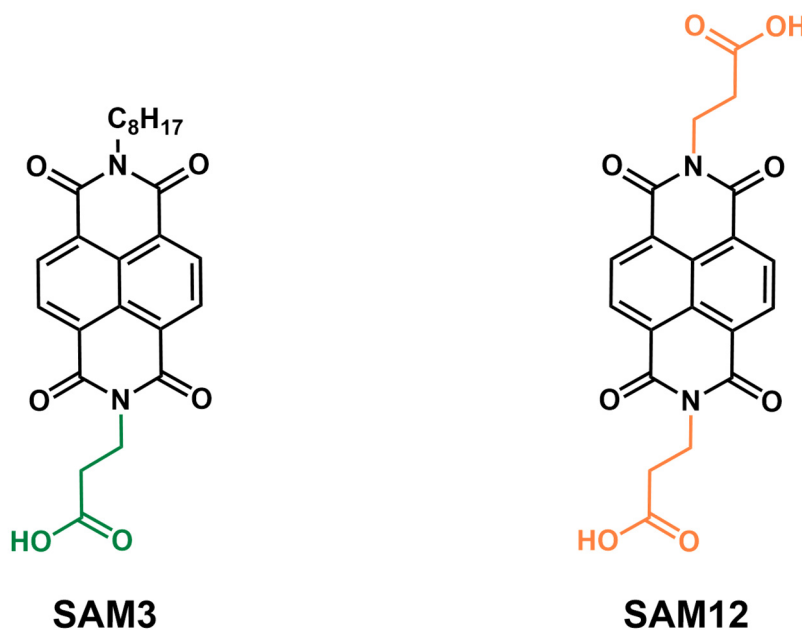


Figure 1. Molecular structures of naphthalene diimide derivatives **SAM3** and **SAM12**.

2. Materials and Methods

2.1. SAMs Synthesis and Characterization

2.1.1. Synthesis of SAM3

1,4,5,8-Naphthalenetetracarboxylic dianhydride (1 g, 3.73 mmol), β -Alanine (0.33 g, 3.70 mmol) and octylamine (0.62 mL, 3.73 mmol) were stirred in dry dimethyl formamide (DMF, 20 mL) at 140 °C under an argon atmosphere. After 16 h, the reaction mixture was cooled to room temperature and then refrigerated for 30 min. The crude was quenched with water and the organic layer was extracted thrice with ethyl acetate, washed with brine and then dried over MgSO₄. The organic extract was filtered, collected and concentrated under reduced pressure. The pure product was obtained using silica gel column chromatography eluting with 10% MeOH in CHCl₃, as a white solid (0.37 g, 22%). Mp: 274–276 °C. ¹H NMR (400 MHz, DMSO) δ 12.41 (s, 1H), 8.58 (s, 4H), 4.30–4.22 (m, 2H), 4.05–3.99 (m, 2H), 2.67–2.60 (m, 2H), 1.65 (q, J = 7.3 Hz, 2H), 1.40–1.20 (m, 10H), 0.90–0.82 (m, 3H). ¹³C NMR (101 MHz, DMSO) δ 172.84, 162.89, 162.84, 130.84, 130.81, 126.66, 126.54, 126.41, 36.53, 32.42, 31.71, 29.16, 29.04, 27.79, 26.99, 22.55, 14.42. MS (ESI+) m/z = 450.1802 [M]⁺ (calculated for C₂₅H₂₆N₂O₆⁺: 450.1791).

2.1.2. Synthesis of SAM12

1,4,5,8-Naphthalenetetracarboxylic dianhydride (1 g, 3.73 mmol) and β -Alanine (0.731 g, 8.205 mmol) were stirred in dry DMF (20 mL) at 140 °C under argon atmosphere. After 16 h, the reaction mixture was cooled to room temperature, dissolved in MeOH and filtered. The crude was concentrated under reduced pressure and precipitated in diethyl ether, filtered and dried under high vacuum to yield the product as a white solid (0.64 g, 42%). mp: >296 °C. ¹H NMR (400 MHz, DMSO) δ 8.59 (s, 4H), 4.30–4.19 (m, 4H), 2.63 (t, J = 7.8 Hz, 4H). ¹³C NMR (101 MHz, DMSO) δ 172.90, 162.85, 130.83, 126.65, 126.43, 36.59, 32.50. MS (ESI+) m/z = 433.0625 [M + Na]⁺ (calculated for C₂₀H₁₄N₂NaO₈⁺: 433.0642).

NMR spectra for both compounds data are provided in the supporting information (Figures S1–S4).

2.2. Device Fabrication

Indium-doped Tin Oxide (ITO)-coated glass substrates, purchased from Xin Yan Technology Ltd. (Kwun Tong, Hong Kong) were used as substrates. They were cleaned using an ultrasonic bath through a sequential immersion for 10 min in an alkaline cleaning solution (Hellmanex soap, Sigma Aldrich, St. Louis, MO, USA), DI water, acetone, and isopropanol (IPA). Subsequently, the ITOs were transferred to UV/ozone equipment for ozone treatment, which was carried out for 30 min, immediately prior to the deposition of the next layer.

2.2.1 For *n-i-p* configuration (ITO/ETL/CdSe@ZnS/PVK/PEDOT:PSS/Al)

SAM3 and **SAM12** as ETL were dissolved in methanol (MeOH) at a concentration of 0.1 mg/mL and left to stand overnight at 50 °C without stirring. The following day, the solution was filtered. Once the ITOs were cleaned and treated with ozone, they were immersed in the SAMs solution overnight at 50 °C. The devices were then rinsed with MeOH to remove the unattached molecules, dried with nitrogen, and subsequently stored in a glovebox for the deposition of commercial CdSe@ZnS quantum dots (QDs, Sigma-Aldrich or Cytodiagnostic, 11.5 ± 0.5 nm particle size, 5 mg/mL in toluene, capped with oleic acid). Each device was coated with 50 μ L of QDs solution via spin coating at 1000 rpm for 60 s, followed by thermal annealing at 100 °C for 20 min. Then, 60 μ L of poly(9-vinylcarbazole) (PVK) solution, prepared at a concentration of 10 mg/mL in 1,4-dioxane, was deposited by spin coating at 3000 rpm for 45 s, followed by thermal annealing at 120 °C for 20 min. Then, the devices were taken out of the glovebox, and 4 drops of a pre-filtered PEDOT:PSS/IPA solution (at 1:1 vol%) were deposited via spin-coating at 7500 rpm for 45 s. The coated samples were then annealed at 150 °C for 20 min. Finally, 100 nm of aluminum were deposited by thermal evaporation under a vacuum of 1 × 10⁻⁶ mbar to complete the device structure which has an active area of 9 mm².

2.2.2 For *p-i-n* configuration (ITO/PEDOT:PSS/poly-TPD/CdSe@ZnS/ETL/Al)

The PEDOT:PSS/IPA solution (1:1 vol%) was sonicated for 5 min, filtered, and deposited on ITO-coated glass substrates via spin-coating at 2000 rpm for 30 s. The coated substrates were annealed at 110 °C for 20 min. Subsequently, the devices were transferred into a glovebox, where an 8 mg/mL poly-TPD solution in chlorobenzene was spin-coated at 2000 rpm for 30 s and thermally annealed at 110 °C for 20 min. Each device

was then coated with 50 μL of QDs solution (Sigma-Aldrich 5 mg/mL in toluene, 11.5 ± 0.5 nm particle size, capped with oleic acid) via spin coating at 1000 rpm for 60 s, followed by thermal annealing at 100 $^{\circ}\text{C}$ for 20 min. Solutions of SAM3 and SAM12 were prepared at a concentration of 0.1 mg/mL in MeOH and spin-coated deposited at 3000 rpm for 30 s without any additional thermal treatment. The deposition of the solutions of SAMs onto the multilayer was performed by three different ways: with a 5-s delay between deposition and the start of the spin coating, in static mode right before starting the spin coating or dynamic, where the solution is deposited when the spin coating is ongoing. A 25 nm layer of TPBi, used as the reference material for the electron transporting layer, was thermally evaporated under a vacuum of 1×10^{-6} mbar. Finally, 100 nm of aluminum were deposited by thermal evaporation under a vacuum of 1×10^{-6} mbar to complete the device structure.

Further information about characterization techniques can be found at the Supplementary Information.

3. Results

3.1. Characterization of the SAM Molecules

The molecules were characterized to determine their optical properties and energy band alignment. The UV-vis absorption and emission spectra were recorded on solutions of the samples in DMF (10^{-5} M) (Figure S5). The emission spectrum was recorded at $\lambda_{\text{exc}} = 381$ nm (maximum of absorption). Both samples have identical optical properties with maxima in absorption at 350 and 381 nm and emission maximum at 450 nm. An optical band gap was calculated from the cut off wavelength ($\lambda_{\text{cut off}}$), see Table 1. According to cyclic voltammetry, the two compounds present a reversible reduction event at around -1.0 V (vs. Fc^+/Fc) and a more complex wave at -1.5 V (Figure S6). The reduction potentials were determined by square wave voltammetry and used to evaluate the electron affinities as $\text{EA (eV)} = -(\text{E}_{\text{RED}} + 4.8)$ eV, which are shown in Table 1. DFT calculations revealed that the calculated LUMOs match the electrochemically determined electron affinities (Figure S7). The fundamental energy gaps were determined from the DFT results and shown in Table 1.

Table 1. Optical properties and energy band alignment of SAM3 and SAM12 estimated in DMF solution.

	$\lambda_{\text{cut off}}$ (nm) ^a	E_{opt} (eV) ^a	EA (eV) ^b	HOMO (eV) ^c	LUMO (eV) ^c	E_{fund} (eV) ^c
SAM3	400	3.1	-3.8	-7.29	-3.66	3.63
SAM12	400	3.1	-3.9	-7.38	-3.75	3.63

^a Values estimated or derived from the UV-vis spectra; ^b Values estimated by square wave voltammetry; ^c Values estimated by DFT calculation.

Moreover, the estimation of the tilting angles reveals that the NDI core is not fully perpendicular to the carboxylic anchoring group, pointing that the SAM will rather be tilted respect to the ITO surface (Figure 2). On the other hand, in the case of SAM12, it is highly unlikely that the molecule anchors to the ITO substrate via the two carboxylic acids. This is due to the considerable bending strain that would be required. Instead, it would rather have a Z-form with the second carboxylic acid group pointing towards the QDs layer on the multi-stacked device configuration.

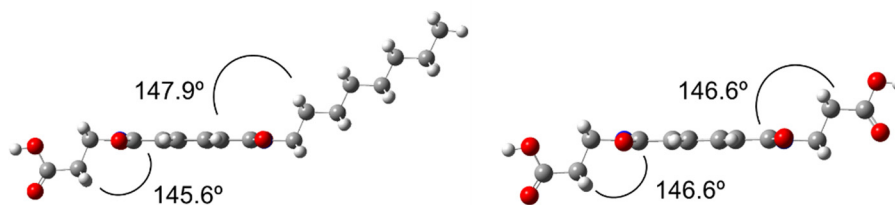


Figure 2. Schematic illustration of the optimized geometry of the SAM3 (left) and SAM12 (right) molecules and the tilting angles formed between the NDI core and the functional moieties.

3.2. Deposition of SAMs onto the ITO Substrate and Construction of n-i-p Devices

Films made of glass/ITO/SAMs were fabricated and characterized using a range of techniques to analyze the surface modifications. Contact angle measurements were carried out to study the surface wettability of the ITO-coated substrates and to identify any changes in the ITO surface caused by the deposition of an additional layer. The water contact angles of ITO/SAM3 and ITO/SAM12 films were estimated to be 104 $^{\circ}$ and 65 $^{\circ}$, respectively (Figure 3). The differences in the contact angles compared to bare ITO (23 $^{\circ}$) confirm that both SAMs were

successfully deposited using bath deposition technique. Additionally, **SAM3** exhibited greater hydrophobicity than **SAM12**, likely due to the direct contact between the long alkyl chains attached to this derivative and the water, confirming the presence of the alkyl chains on the top of the SAM layer. This increased hydrophobicity can significantly influence the formation of the films of QDs, a factor that will be further analysed using the atomic force microscope (AFM) technique. The study of the surface of the substrate after the deposition of the SAMs shows that the pattern is similar in all cases, indicating a homogeneous and uniform coverage. However, the roughness mean square (RMS) values differ slightly from 2.7 nm of ITO and **SAM3** to 2.4 nm for **SAM12**, respectively. The lower RMS of **SAM12** suggests a more uniform monolayer formation on ITO.

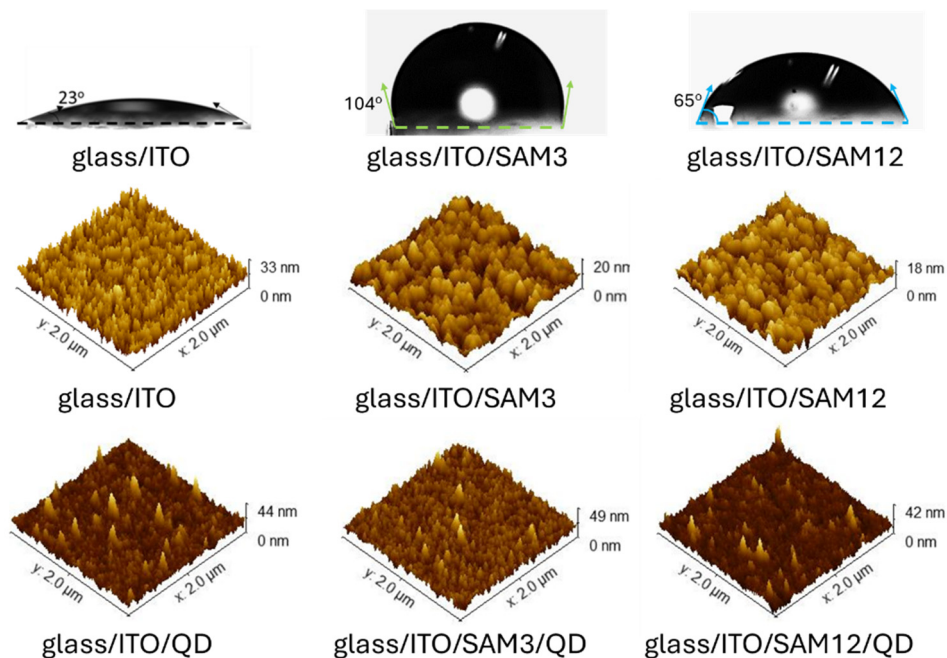


Figure 3. Contact angle measurements of water on ITO, ITO/**SAM3** and ITO/**SAM12** surfaces (**top**); images of AFM of the ITO surface and the hole selective contacts, deposited onto ITO/**SAM3** and ITO/**SAM12** and of the QD films deposited onto ITO, ITO/**SAM3** and ITO/**SAM12**.

To further corroborate the surface modification of ITO by SAM molecules, we employed X-ray photoelectron spectroscopy (XPS). The formation of a chemical bond between SAMs and ITO is confirmed by the shift in the binding energy of the peaks corresponding to In 3d and Sn 3d on the ITO/SAMs compared to those on bare ITO (Figure S8a,b). Moreover, both SAMs displayed a consistent peak at 400.2 eV in the N 1s region, assigned to the imide (C=O)–N–(C=O) bonds, which are not observed on the ITO substrate (see Figure S8c). On the other hand, the C 1s spectra recorded on ITO were deconvoluted into distinct peaks, corresponding to C–C or C–H at 284.8 eV, C–O or C–N at 286 eV, and 289.1 eV assigned to satellite π – π^* , all of them arising from adventitious carbon (Figure S9). The measurement on ITO/SAM films revealed the presence of the C–C peak at 284.8 eV, the C–O or C–N peak at 286.1 eV, a new peak not observed on ITO due to C=O/O–C=O at 288.3 eV and a fourth peak at 290.6 eV due to adventitious carbon for **SAM3** and **SAM12**, respectively (Figure S9). As expected, the atomic concentration of carbon is higher in **SAM3** in comparison to **SAM12** whereas the concentration of oxygen is lower (Table S1). Regarding the O 1s spectra, peaks were observed for the oxygen lattice in ITO at 529.9 and 529.8 eV, for C=O at 532.5 and for C–O at 533.4 and 533.2 eV for **SAM3** and **SAM12**, respectively. The bare ITO substrate also presented three peaks: one at 530 eV from the oxygen lattice in ITO, and two peaks at 531 eV of C=O, and 532.9 eV from C–OH eV (see Figure S8 and Table S1), where the carbon compounds are presumably coming from cleaning residues or environmental contaminants.

Once the coverage of the ITO by the SAMs had been assessed, we turned to the characterization of the ITO/SAM/QD films. AFM analysis of ITO covered with QDs showed heterogeneous coverage with the presence of aggregates, and slightly higher RMS compared to the bare ITO film (4.2 vs. 2.7 nm, respectively). When the QDs are spin-coated onto the ITO/SAM substrates, the resulting films also contain some aggregates, Figure 3. The RMS values increase in comparison to the values detected onto ITO/SAM, especially in the case of ITO/**SAM3**/QD. However, the QDs film on ITO/**SAM12** shows a lower roughness of 3.3 nm compared to that on ITO/**SAM3** (4.7 nm). This suggests that **SAM12** promotes a more uniform deposition of QDs, which would

improve film morphology. The electron mobility (μ_e) of the SAMs has been measured on electron-only devices with the architecture ITO/SAM/QD/TPBi/Ag and estimated by the space charge limited current (SCLC) method by Equation (S1). One control device without SAMs has been prepared as a reference. The μ_e was found to be 4.3×10^{-5} and 2.9×10^{-5} $\text{cm}^2/\text{V}\cdot\text{s}$ for **SAM3** and **SAM12**, respectively, which is lower than the value found on the reference of 4.5×10^{-4} $\text{cm}^2/\text{V}\cdot\text{s}$ for the ITO. Overall, we estimate that the perpendicular configuration of the SAMs onto the ITO electrode permits the interaction of the ligands with the surface of the QD but avoids the π - π stacking of the NDI core with the ITO, which is reflected in the lower electron mobility values.

Steady-state and PL time decay measurements were employed to investigate the interface between SAMs and CdSe@ZnS quantum dots. As shown in Figure 4a, the highest emission intensity corresponds to the ITO/QDs film, while the spectra for films with **SAM3** and **SAM12** exhibited significant quenching in their emission. The maximum of the emission band is 648 nm for all the samples, whereas the full-width half maximum (FWHM) is 25.1 nm, values that are similar in all the samples. The decay lifetime of the samples has been measured by time-correlated single photon counting (TCSPC) after excitation at 405 nm, recording at 650 nm and acquisition of 5000 cps (Figure 4b). The decays are fitted to a biexponential equation (Equation S2) where the faster decay is assigned to processes occurring at surface-related traps and the slower decay is assigned to radiative recombination transitions in internal defect states within the QDs [26,27]. The estimation of the average lifetime has been done according to Equation (S3) and shows that the PL decay is shorter for the ITO/SAMs/QDs (see Table S2). A closer inspection of the decay processes reveals that the number of events in the faster process increases in the SAM-containing films in comparison to ITO/QDs samples while the decay lifetime of the slower process accelerates. This is more evident for **SAM3**, suggesting to an effect of the alkyl moiety on the surface of the CdSe/ZnS that is not observed for the $-\text{COOH}$ group present on **SAM12**.

In order to study the possible effect on the surface, ligand exchange tests have been done in polar (MeOH) and non-polar solvents (toluene) mixing **SAM3** and the QDs in solutions, however, no clear shift was observed in any of the two reactions (see Figure S10). Therefore, our hypothesis is that the changes in the decay lifetimes are due to the partial ligand exchange on the surface of the QDs by the functional moieties of the SAMs, which neither affect the dispersion of the QDs in solution nor the formation of aggregates in films, but is reflected in the fluorescence quenching [28].

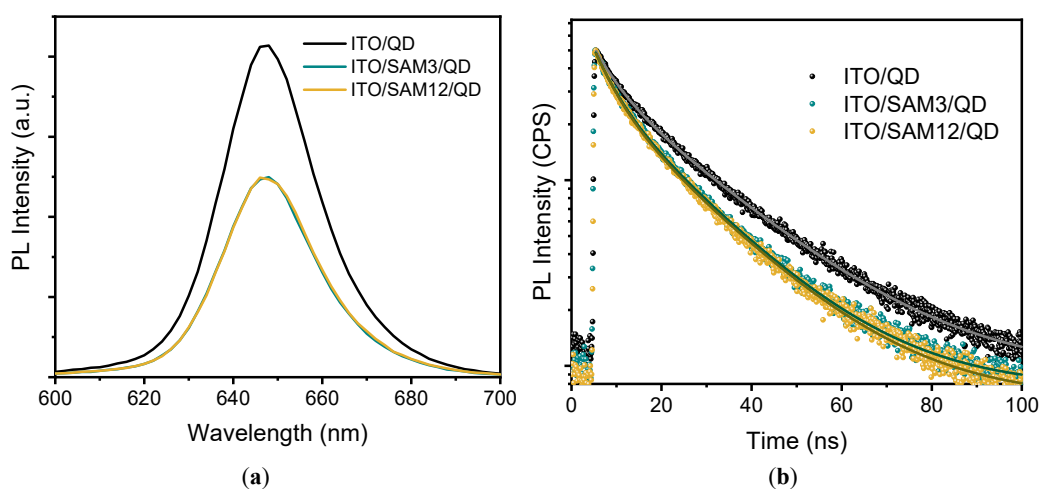


Figure 4. PL emission spectra of glass/ITO/ETL/QDs films after excitation at 405 nm (a) and the corresponding PL decay after acquisition of 5000 cps recorded at 650 nm (b). The continuous line represents the fitting of the decay to the biexponential Equation (S2).

The next step was the fabrication of light-emitting devices using the NDI-based SAMs as electron-selective contacts (Figure 5). The architecture of the device followed the *n-i-p* scheme, where the electron transport material is deposited onto the ITO, sandwiching the photoactive QD layer with the hole transport material made by PVK and PEDOT:PSS and topped with the metallic electrode of aluminum. The energy level of the SAMs are adequate to act as electron selective contacts: the HOMO level is deep enough to block the holes in the emissive layer whereas the LUMO levels permit the injection of electrons into the QDs. The performance of devices prepared with **SAM3** and **SAM12** was compared with devices without electron selective contact as reference. Measurement of the variation of luminance and current density with applied bias are shown in Figure 5 and described in Table S3.

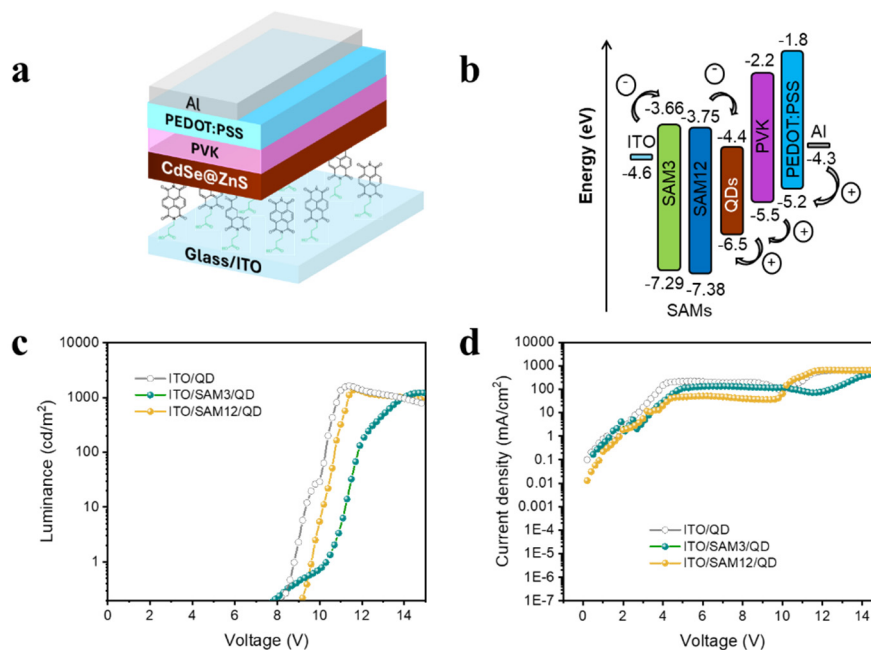


Figure 5. Schematic representation of SAM-based LED device architecture (a), energy levels of all the materials involved in the device configuration (b), luminance (c) and current density (d) dependence with applied bias in *n-i-p* devices. Compliance at 0.2 A was used in the measurements, which accounts for the saturation of the current density at voltage values above 12 V for the ITO/QD and ITO/SAM12/QD devices.

Light emission occurs at bias above 7 V, reaching maximum values at 11 V for reference and SAM12 and at 14 V for SAM3. It is worth mentioning that the presence of SAMs induces lower current densities at lower voltages compared to the bare ITO, due to the higher LUMO level acting as an effective electron-blocking layer for injection, whereas SAM3 reduces the current density at higher voltages. Despite the luminance values are similar between SAM12 and the reference, the deviation in the maximum luminance values obtained is reduced in the case of SAM12 pointing towards more reproducible devices (Figure S11a).

The higher luminance of SAM12 in contrast to SAM3 can be assigned to the more adequate levels of the HOMO/LUMO, to the smoother surface formed by the QDs on top of the former and the lower PL quenching, pointing towards the importance of achieving a good dispersion in the photoactive film and the interaction with surface ligands. However, higher current densities are required in SAM12-devices to achieve higher luminance values, which is translated into lower values of current efficiency (Figure S11b).

3.3. Application of SAM3 and SAM12 in *p-i-n* Configuration

The SAMs have also been tested in the *p-i-n* structure where the electron selective contact is deposited onto the photoactive layer (Figure 6a,b). In order to assess the charge kinetics in these systems, photoluminescence and PL decay measurements were employed to investigate the interface between SAMs and CdSe@ZnS quantum dots. The samples studied included ITO/QDs and ITO/QDs/ETL, where the electron selective contacts were either SAM3, SAM12, or TPBi (used as a reference). The PL emission spectra reveal a maximum emission band at the range of 648 nm for all the samples (Figure S12a). The PL decays, depicted in Figure S12b, show that the ITO/QDs/TPBi sample lifetime was longer than the neat QDs film. In addition, the presence of SAMs increases the percentage of nonradiative processes on the surface and reduces the fluorescence lifetime decays. In comparison to the ITO/SAM/QDs configuration, the average decay lifetimes are shorter.

To get additional information about the role played by the SAMs on the devices, we studied different conditions for the SAMs deposition. Solutions of SAM3 and SAM12 were prepared in MeOH and stirred overnight at room temperature. The next day, the solutions were filtered and spin coated on the QDs by three different strategies described the experimental section: the 5 s delay before spinning, static deposition and deposition during spinning (dynamic mode). As a reference, 25 nm of TPBi were evaporated. The performance of the devices, with structure ITO/PEDOT:PSS/polyTPD/QD/SAM/Al shown in Figures S13 and S14 indicates that the deposition in dynamic mode offers higher luminance values for both SAM3 and SAM12 whereas spinning after a 5 s delay or deposition in static conditions do not show significant differences among them. It is worth mentioning that the current density values are not significantly affected by the deposition method. The comparison

of the devices prepared in dynamic mode indicates that devices prepared with **SAM12** have more luminance than those prepared with **SAM3**, but are lower than the TPBi reference (Figure 6c and Table S5), probably due to the quenching of light emission observed by TCSPC.

The higher luminance and the lower current density of the TPBi reference results in higher EQE, whereas **SAM3** and **SAM12** show similar results at high current densities (Figure S15a). Finally, the EL spectra show a peak at 665 nm in all the devices (Figure S15b). The 20 nm redshift observed for all the devices in comparison to the PL measurements is assigned to the electric-field induced Stark effect [29]. In comparison to *n-i-p* architecture, the turn-on voltage values are lower, due to the more effective energy level alignment between the materials that leads to lower current density values. The bias dependence of current density is similar for **SAM3** and **SAM12** devices, Figure 6d. Therefore, in both the *n-i-p* and *p-i-n* configurations, the **SAM12** offers higher luminance values at the expense of higher current density values which cause lower efficiency values than for **SAM3**. Despite both SAMs quenching the light emission from the QDs, in the case of **SAM12**, the decrease in the lifetime decay is less pronounced than for **SAM3**, whose long alkyl chain can interact through ligand exchange with the surface of the QDs. On the other hand, the higher LUMO level of **SAM3** modulates the electron injection into the emissive layer, which favours the efficiency of the devices.

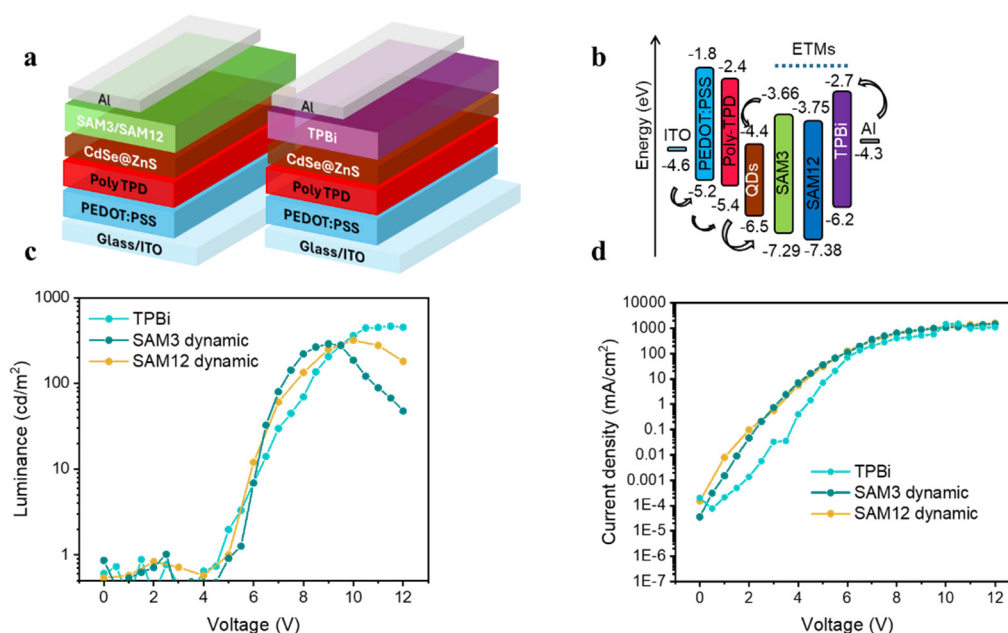


Figure 6. Schematic representation of SAM-based LED device architecture (a), energy levels of all the materials involved in the device configuration (b), luminance (c) and current density (d) dependence with applied bias in the *p-i-n* devices.

Overall, the performance of the light emitting devices depends on a number of factors such as: (i) the composition of the photoemissive material, that determine the wavelength of the colour emission, (ii) the nature of the charge transport materials which is directly related to the carrier mobility and to the quality of the film deposited on top, (iii) the presence of defects at the interface that can act as charge traps reducing the radiative recombination, or as local points for charge accumulation that lead to charge imbalance, and (iv) the energy level alignment of the materials that affect the injection barriers [25,30]. All these factors (the injection barrier, the carrier mobility and the density of charge traps) influence the charge balance which in turn determines the turn on voltage, the maximum luminance and the external quantum efficiency [15]. On the other hand, electron injection in CdSe/ZnS devices is more efficient than hole injection, so in order to reduce the electron injection rate, the insertion of electron blocking layers between the electron transport material and the emissive layer have been tested and reported [31]. The incorporation of electron selective SAMs in CdSe/ZnS has influenced the factors mentioned above resulting in functional devices, despite their moderate performance. Thus, further exploration of the thickness of the photoemissive materials and the hole transport layers and the quality of the films would benefit charge balance in the devices and increase light emission, enhancing the performance of the devices.

4. Conclusions

We have prepared proof-of-concept devices in which NDI derivatives have been applied for the first time as electron selective contacts in quantum dot-based light-emitting diodes. The synthesized molecules differ in their functional moieties, which have demonstrated a crucial effect on the formation of the QD film and the performance of the devices. For example, **SAM12** shows higher luminance in both *n-i-p* and *p-i-n* configurations, which is attributed to the smoother formation of the QD film and lower quenching of light emission compared to **SAM3**. On the other hand, the long alkyl chain of **SAM3** interacts with the surface of the QDs, reducing the fluorescence lifetime decay. However, the LUMO level acts as a barrier for excessive electron injection, modulating the current density and achieving better efficiencies.

Therefore, in this work, we have demonstrated the application of NDI derivatives as electron selective contacts, which establishes a foundation for further research into the underexplored field of electron selective SAMs in optoelectronic devices.

Supplementary Materials

The additional data and information can be downloaded at: <https://media.scilitp.com/articles/others/2506101422321358/MatSus-1232-SI-for-online.pdf>. Figure S1: ^1H NMR of **SAM3** in *d6*-DMSO. Figure S2: ^{13}C NMR of **SAM3** in *d6*-DMSO. Figure S3: ^1H NMR of **SAM12** in *d6*-DMSO. Figure S4: ^{13}C NMR of **SAM12** in *d6*-DMSO. Figure S5: UV-vis (black) and fluorescence (red) spectra of (a) **SAM3** and (b) **SAM12** in DMF solution ($C = 5 \times 10^{-5}$ M). The excitation wavelength for the fluorescence measurements was fixed at 381 nm. Figure S6: Cyclic voltammetry of (a) **SAM3** and (b) **SAM12** measured in anhydrous DMF ($C = 5 \times 10^{-4}$ M), using a Pt disk working electrode, a Pt curly wire auxiliary electrode and a silver wire pseudo-reference electrode. TBAPF₆ was used as a supporting electrolyte ($C = 0.1$ M) and the results were referenced to the Fc⁺/Fc redox potential. Figure S7: HOMO and LUMO of **SAM3** and **SAM12** estimated by DFT calculations. Figure S8: XPS high-resolution spectra of (a) In 3d and (b) Sn 3d and survey spectra of (c) ITO, (d) ITO/**SAM3** and (e) ITO/**SAM12** films. Figure S9: XPS high-resolution survey spectra of O1s and C1s on ITO, ITO/**SAM3** and ITO/**SAM12**. Figure S10: PL spectra of the solutions of QD in toluene and QD mixed with **SAM3** in toluene or in methanol after excitation at 450 nm. Figure S11: (a) Luminance statistics for *n-i-p* devices, and (b) Variation of current efficiency with applied bias in *n-i-p* devices. Figure S12: PL emission spectra (a) and PL emission decays (b) of ITO/QDs and ITO/QDs/ETLs films after excitation at 405 nm and acquisition of 5000 cps at 650 nm. The continuous line represents the fitting of the decay to the biexponential Equation (S2). Figure S13: Luminance (a) and current density dependence (b) with applied bias for *p-i-n* devices prepared with **SAM3** deposited under different conditions. Figure S14: Luminance (a) and current density dependence (b) with applied bias for *p-i-n* devices prepared with **SAM12** deposited under different conditions. Figure S15: (a) EQE and (b) EL spectra for *p-i-n* devices. Table S1: XPS elemental quantification from the XPS measurements of SAMs coated on ITO and bare ITO. Table S2: PL lifetime decay of the ITO/ETL/QD films measured after excitation at 405 nm, recorded at 650 nm after acquisition of 5000 cps. The quality of the fitting is described by the χ^2 parameter. Table S3: Optoelectronic characterization of the devices where **SAM3** and **SAM12** are tested as electron selective contacts in *n-i-p* configuration in LEDs. Table S4: PL lifetime decay of the ITO/QD/ETL films measured after excitation at 405 nm and acquisition at 650 nm for 5000 cps. The quality of the fitting is described by the χ^2 parameter. Table S5: Optoelectronic characterization of the *p-i-n* devices where **SAM3** and **SAM12** have been deposited in dynamic mode. Reference [32] is cited in the supplementary Materials.

Author Contributions

Conceptualization, G.C., E.P. and E.M.-F.; synthesis and characterization of **SAM3** and **SAM12**: A.S., M.C. and D.W.; formal analysis of the generated data: M.M., J.G.S., M.C. and E.M.-F.; preparation and characterization of LEDs: M.M., M.G., A.D.V., L.M.-M., J.G.S., A.S., F.P. and R.S.S.; resources, I.M.-S., G.C., E.P. and E.M.-F.; writing—original draft preparation, M.M., A.S. and J.G.S.; writing—review and editing, M.M., J.G.S., R.S.S., I.M.-S., E.P., G.C. and E.M.-F.; supervision, I.M.-S., G.C., E.P. and E.M.-F.; funding acquisition, G.C., E.P. and E.M.-F. All authors have read and agreed to the published version of the manuscript.

Funding

This work is funded by the Ministerio de Ciencia e Innovación of the Spanish government through projects Severo Ochoa Grant MCIN/AEI/10.13039/501100011033 (CEX2019-000925-S), ElectroVolt PID2022-139866NB-I00 and by Generalitat Valenciana by the project Q-Solutions (CIPROM/2021/078) via PROMETEO program.

Data Availability Statement

Data is available from the corresponding authors upon reasonable request.

Acknowledgments

Diana Tahuilán is acknowledged for the estimation of the tilting angles of SAMs by DFT calculations. Funding is from Ministerio de Ciencia e Innovación through projects Severo Ochoa Grant MCIN/AEI/10.13039/501100011033 (CEX2019-000925-S), ElectroVolt PID2022-139866NB-I00 and by Generalitat Valenciana by the project Q-Solutions (CIPROM/2021/078) via PROMETEO program is acknowledged. E.P. also acknowledges ICIQ, CERCA, and ICREA for financial support. GC thanks the Leverhulme Trust for the award of a research fellowship.

Conflicts of Interest

The authors declare no conflict of interest.

References

1. Han, P.; Zhang, Y. Recent Advances in Carbazole-Based Self-Assembled Monolayer for Solution-Processed Optoelectronic Devices. *Adv. Mater.* **2024**, *36*, 2405630. <https://doi.org/10.1002/adma.202405630>.
2. Li, W.; Martínez-Ferrero, E.; Palomares, E. Self-Assembled Molecules as Selective Contacts for Efficient and Stable Perovskite Solar Cells. *Mater. Chem. Front.* **2023**, *8*, 681–699. <https://doi.org/10.1039/d3qm01017a>.
3. Suo, J.; Yang, B.; Bogachuk, D.; et al. The Dual Use of SAM Molecules for Efficient and Stable Perovskite Solar Cells. *Adv. Energy Mater.* **2025**, *15*, 2400205. <https://doi.org/10.1002/aenm.202400205>.
4. Al-Ashouri, A.; Köhnen, E.; Li, B.; et al. Monolithic Perovskite/Silicon Tandem Solar Cell with >29% Efficiency by Enhanced Hole Extraction. *Science* **2020**, *370*, 1300–1309. <https://doi.org/10.1126/science.abd4016>.
5. Puerto Galvis, C.E.; González Ruiz, D.A.; Martínez-Ferrero, E.; et al. Challenges in the Design and Synthesis of Self-Assembling Molecules as Selective Contacts in Perovskite Solar Cells. *Chem. Sci.* **2023**, *15*, 1534–1556. <https://doi.org/10.1039/d3sc04668k>.
6. Wang, X.; Li, J.; Guo, R.; et al. Regulating Phase Homogeneity by Self-Assembled Molecules for Enhanced Efficiency and Stability of Inverted Perovskite Solar Cells. *Nat. Photonics* **2024**, *18*, 1269–1275. <https://doi.org/10.1038/s41566-024-01531-x>.
7. Lin, J.Y.; Hsu, F.C.; Chang, C.Y.; et al. Self-Assembled Polar Hole-Transport Monolayer for High-Performance Perovskite Photodetectors. *J. Mater. Chem. C* **2021**, *9*, 5190–5197. <https://doi.org/10.1039/d1tc00433f>.
8. Sasaki, Y.; Minami, T. Organic Field-Effect Transistors for Interfacial Chemistry: Monitoring Reactions on SAMs at the Solid-Liquid Interface. *ACS Appl. Mater. Interfaces* **2025**, *17*, 31165–31173. <https://doi.org/10.1021/acsami.5c00297>.
9. Zheng, H.; Zhang, F.; Zhou, N.; et al. Self-Assembled Monolayer-Modified ITO for Efficient Organic Light-Emitting Diodes: The Impact of Different Self-Assemble Monolayers on Interfacial and Electroluminescent Properties. *Org. Electron.* **2018**, *56*, 89–95. <https://doi.org/10.1016/j.orgel.2018.01.038>.
10. Li, L.; Luo, Y.; Wu, Q.; et al. Efficient and Bright Green InP Quantum Dot Light-Emitting Diodes Enabled by a Self-Assembled Dipole Interface Monolayer. *Nanoscale* **2023**, *15*, 2837–2842. <https://doi.org/10.1039/d2nr06618a>.
11. Shin, Y.S.; Ameen, S.; Oleiki, E.; et al. A Multifunctional Self-Assembled Monolayer for Highly Luminescent Pure-Blue Quasi-2D Perovskite Light-Emitting Diodes. *Adv. Opt. Mater.* **2022**, *10*, 2201313. <https://doi.org/10.1002/adom.202201313>.
12. Chen, B.; Guo, R.; He, Z.; et al. Self-Assembled Monolayers as Hole Transport Layers for Efficient Thermally Evaporated Blue Perovskite Light-Emitting Diodes. *Chem. Eng. J.* **2023**, *476*, 146476. <https://doi.org/10.1016/j.cej.2023.146476>.
13. Gkeka, D.; Hamilton, I.; Stavridis, T.; et al. Tuning Hole-Injection in Organic-Light Emitting Diodes with Self-Assembled Monolayers. *ACS Appl. Mater. Interfaces* **2024**, *16*, 39728–39736. <https://doi.org/10.1021/acsami.4c08088>.
14. Lin, J.Y.; Hsu, F.C.; Chao, Y.C.; et al. Self-Assembled Monolayer for Low-Power-Consumption, Long-Term-Stability, and High-Efficiency Quantum Dot Light-Emitting Diodes. *ACS Appl. Mater. Interfaces* **2023**, *15*, 25744–25751. <https://doi.org/10.1021/acsami.3c01566>.
15. Li, Z.; Chen, Z.; Shi, Z.; et al. Charge Injection Engineering at Organic/Inorganic Heterointerfaces for High-Efficiency and Fast-Response Perovskite Light-Emitting Diodes. *Nat. Commun.* **2023**, *14*, 6441. <https://doi.org/10.1038/s41467-023-41929-9>.
16. Kumari, S.; Imran, M.; Aktas, E.; et al. Self-Assembled Molecules as Selective Contacts in CsPbBr₃ Nanocrystal Light Emitting Diodes. *J. Mater. Chem. C* **2023**, *11*, 3788–3795. <https://doi.org/10.1039/D2TC03536G>.
17. Kumar, K.; Karmakar, A.; Thakur, D.; et al. Self-Assembled Molecular Network with Waterwheel-like Architecture: Experimental and Theoretical Evaluation toward Electron Transport Capabilities for Optoelectronic Devices. *Phys. Chem. Chem. Phys.* **2024**, *26*, 11922–11932. <https://doi.org/10.1039/d4cp00390j>.
18. Giovannitti, A.; Nielsen, C.B.; Sbircea, D.T.; et al. N-Type Organic Electrochemical Transistors with Stability in Water. *Nat. Commun.* **2016**, *7*, 13066. <https://doi.org/10.1038/ncomms13066>.
19. Lee, G.S.; Oh, J.G.; Suh, E.H.; et al. Naphthalene-Diimide-Based Small Molecule Containing a Thienothiophene Linker for

- n-Type Organic Field-Effect Transistors. *Macromol. Res.* **2022**, *30*, 470–476. <https://doi.org/10.1007/s13233-022-0054-4>.
20. Li, L.; Wu, Y.; Li, E.; et al. Self-Assembled Naphthalimide Derivatives as an Efficient and Low-Cost Electron Extraction Layer for n-i-p Perovskite Solar Cells. *Chem. Commun.* **2019**, *55*, 13239–13242. <https://doi.org/10.1039/c9cc06345e>.
 21. Liao, Q.; Kang, Q.; Yang, Y.; et al. Highly Stable Organic Solar Cells Based on an Ultraviolet-Resistant Cathode Interfacial Layer. *CCS Chem.* **2022**, *4*, 938–948. <https://doi.org/10.31635/ccschem.021.202100852>.
 22. Rozanski, L.J.; Castaldelli, E.; Sam, F.L.M.; M et al. Solution Processed Naphthalene Diimide Derivative as Electron Transport Layers for Enhanced Brightness and Efficient Polymer Light Emitting Diodes. *J. Mater. Chem. C* **2013**, *1*, 3347–3352. <https://doi.org/10.1039/c3tc30175c>.
 23. Jameel, M.A.; Yang, T.C.J.; Wilson, G.J.; et al. Naphthalene Diimide-Based Electron Transport Materials for Perovskite Solar Cells. *J. Mater. Chem. A* **2021**, *9*, 27170–27192. <https://doi.org/10.1039/d1ta08424k>.
 24. Cho, I.; Kim, G.Y.; Kim, S.; et al. Naphthalene Diimide-Modified SnO₂ Enabling Low-Temperature Processing for Efficient ITO-Free Flexible Perovskite Solar Cells. *Small* **2024**, *20*, 2402425. <https://doi.org/10.1002/sml.202402425>.
 25. Jang, E.; Jang, H. Review: Quantum Dot Light-Emitting Diodes. *Chem. Rev.* **2023**, *123*, 4663–4692. <https://doi.org/10.1021/acs.chemrev.2c00695>.
 26. Li, L.; Pandey, A.; Werder, D.J.; et al. Efficient Synthesis of Highly Luminescent Copper Indium Sulfide-Based Core/Shell Nanocrystals with Surprisingly Long-Lived Emission. *J. Am. Chem. Soc.* **2011**, *133*, 1176–1179. <https://doi.org/10.1021/ja108261h>.
 27. Mandal, G.; Darragh, M.; Wang, Y.A.; et al. Cadmium-Free Quantum Dots as Time-Gated Bioimaging Probes in Highly-Autofluorescent Human Breast Cancer Cells. *Chem. Commun.* **2013**, *49*, 624–626. <https://doi.org/10.1039/c2cc37529j>.
 28. Hoppe, C.E.; Williams, R.J.J. Tailoring the Self-Assembly of Linear Alkyl Chains for the Design of Advanced Materials with Technological Applications. *J. Colloid Interface Sci.* **2018**, *513*, 911–922. <https://doi.org/10.1016/j.jcis.2017.10.048>.
 29. Mashford, B.S.; Stevenson, M.; Popovic, Z.; et al. High-Efficiency Quantum-Dot Light-Emitting Devices with Enhanced Charge Injection. *Nat. Photonics* **2013**, *7*, 407–412. <https://doi.org/10.1038/nphoton.2013.70>.
 30. Kim, S.K.; Yang, H.; Kim, Y.S. Control of Carrier Injection and Transport in Quantum Dot Light Emitting Diodes (QLEDs) via Modulating Schottky Injection Barrier and Carrier Mobility. *J. Appl. Phys.* **2019**, *126*, 185702. <https://doi.org/10.1063/1.5123670>.
 31. Li, D.; Bai, J.; Zhang, T.; et al. Blue Quantum Dot Light-Emitting Diodes with High Luminance by Improving the Charge Transfer Balance. *Chem. Commun.* **2019**, *55*, 3501–3504. <https://doi.org/10.1039/C9CC00230H>.
 32. Frisch, M.J.; Trucks, G.W.; Schlegel, H.B.; et al. *Gaussian 09, Revision A.02*; Gaussian, Inc.: Wallingford, CT, USA, 2016.